Inorganic Chemistry

Article

pubs.acs.org/IC

Improving the Photosensitizing Properties of Ruthenium Polypyridyl Complexes Using 4-Methyl-2,2′-bipyridine-4′-carbonitrile as an Auxiliary Ligand

Juan H. Mecchia Ortiz,[†] Nadia Vega,[‡] David Comedi,[‡] Mónica Tirado,[‡] Isabel Romero,[§] Xavier Fontrodona,[§] Teodor Parella,[∥] F. Eduardo Morán Vieyra,[⊥] Claudio D. Borsarelli,[⊥] and Néstor E. Katz[†,*]

[†]INQUINOA-CONICET, Instituto de Química Física, Facultad de Bioquímica, Química y Farmacia, Universidad Nacional de Tucumán, Ayacucho 491, (T4000INI) San Miguel de Tucumán, Argentina

[‡]LAFISO and LPDM, Facultad de Ciencias Exactas y Tecnología, Universidad Nacional de Tucumán, Avda. Independencia 1800, (T4002BLR) San Miguel de Tucumán, Argentina

[§]Departament de Química and Serveis Tècnics de Recerca (STR), Universitat de Girona, Campus de Montilivi, E-17071 Girona, Spain

[∥]Servei de RMN, Universitat Autònoma de Barcelona, Bellaterra E-08193, Barcelona, Spain

[⊥]Laboratorio de Cinética y Fotoquímica, Centro de Investigaciones y Transferencia de Santiago del Estero (CITSE-CONICET), Universidad Nacional de Santiago del Estero, RN 9, Km 1125, (4206) Santiago del Estero, Argentina

Supporting Information

ABSTRACT: We report in this work the synthesis and spectroscopic, electrochemical, spectroelectrochemical, and photophysical characterization of a novel series of ruthenium polypyridyl complexes with 4-methyl-2,2′-bipyridine-4′-carbonitrile (Mebpy-CN) as an auxiliary ligand of general formula $[Ru(bpy)_{3-x}(Mebpy\text{-}CN)_x](PF_6)_2$ (x = 1−3) (with bpy = 2,2′-bipyridine). A significant increase in the lifetime and quantum yield of emission of the lowest ^{3}MLCT excited state is disclosed when going from x = 1 to x = 3, evidencing an improvement of the photosensitizing properties with respect to $[Ru(bpy)_3](PF_6)_2$. Furthermore, quenching by molecular oxygen of ^{3}MLCT excited states of the three complexes produced singlet molecular oxygen ($^1O_2$) with quantum yield values higher than that of $[Ru(bpy)_3]^{2+}$ in CH_3CN. The structure of the complex with x = 1 has been determined by X-ray diffraction. The photoconductivity of ZnO nanowires covered with this same complex is increased by an order of magnitude, pointing to its feasibility as a component of a DSSC. A new dinuclear complex with Mebpy-CN as a bridging ligand has also been prepared and characterized by physicochemical techniques. The derived mixed-valent species of formula $[(bpy)_2Ru^{II}(Mebpy\text{-}CN)Ru^{III}(NH_3)_5]^{5+}$ displays a considerable metal−metal electronic coupling due to the delocalization effect of a nitrile group in the 4′ position of the bpy ring.

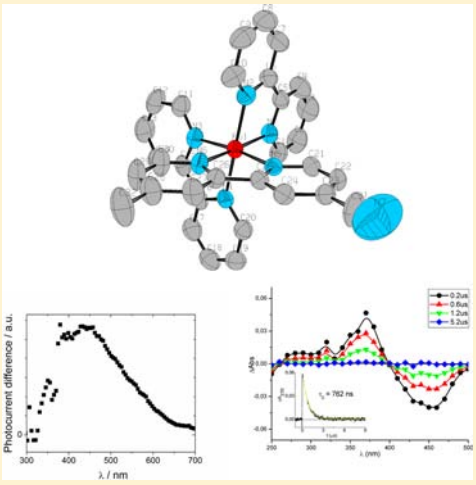

INTRODUCTION

Design and development of efficient energy conversion devices is relevant in response to increasing global energy demands. Ruthenium polypyridyl complexes have been extensively studied in relation to conversion processes of solar into electrical energy, due to their excellent properties as photosensitizers.[1] In particular, their high absorptivity in the visible region, the long lifetimes of their lowest energy triplet excited states, and their relatively high thermal stability have led to their use in dye-sensitized solar cells (DSSCs), of Grätzel's type.[2] By judiciously choosing nanoscale properties, a third generation of solar cells will promptly be developed.[3,4]

One of the important issues to be considered in improving the photoelectrochemical performance of the solar cell is the interaction between the dye and the semiconductor surface.[5] Carboxyl groups are the usual anchoring entities for chemical adsorption of the dye over the metal oxide surface, and TiO_2 is the semiconductor usually employed. In this work, we address the possibility of designing novel solar cells using nitrile groups as anchoring entities and ZnO nanowires as semiconductors. Metal cyanide complexes are known to sensitize TiO_2 nanoparticles through monodentate binding of a nitrile group

Received: November 27, 2012
Published: April 10, 2013

   dx.doi.org/10.1021/ic302594b | *Inorg. Chem.* 2013, 52, 4950−4962

to a surface Ti^{IV} site,[6] while ZnO is a promising material to be incorporated in DSSCs.[3] Moreover, sensitizers with anchoring groups without protons are preferred in ZnO solar cells, due to precipitation of dye molecules.[3] We report here the synthesis and exhaustive physicochemical characterization of new ruthenium polypyridyl complexes (**1**−**3**) of formula $[Ru(bpy)_{3-x}(Mebpy\text{-}CN)_x](PF_6)_2$, (bpy = 2,2′-bipyridine, Mebpy-CN = 4-methyl-2,2′-bipyridine-4′-carbonitrile, x = 1 (**1**), 2 (**2**), 3 (**3**)) that can be used as photosensitizers onto ZnO nanowires. These complexes have a nitrile group in the periphery of one of the polypyridyl ligands which can envisaged as an anchoring group while preserving the integrity of the nanowires.[5,7] It was hoped that the photosensitizing properties can be improved with increasing substitution of bpy by Mebpy-CN. Indeed, recent work by McCusker et al.[8] has evidenced that the lifetimes of excited states can be increased by increasing the number of nitrile groups in the series $[Ru(bpy)_{3-n}(CN\text{-}Me\text{-}bpy)_n](PF_6)_2$ (where CN-Me-bpy = 4,4′-dicyano-5,5′-dimethyl-2,2′-bipyridine, n = 1−3).

Besides, since a nitrile group can be coordinated through its free N to another metal moiety in solution, new models relevant for intramolecular electron transfer processes which may be used in artificial photosynthesis can be designed; therefore, we also report in this work the synthesis and complete physicochemical characterization of a new dinuclear isovalent species of formula $[(bpy)_2Ru^{II}(Mebpy\text{-}CN)\text{-}Ru^{II}(NH_3)_5](PF_6)_4$ and its mixed-valent derivative in CH_3CN solution, the ion $[(bpy)_2Ru^{II}(Mebpy\text{-}CN)Ru^{III}(NH_3)_5]^{5+}$. The Marcus−Hush model was applied to this last complex in order to assess the degree of metal-to-metal electronic coupling imposed by the Mebpy-CN ligand, to be compared to that of a previously studied bridging ligand, 5-CNphen (5-CNphen = 5-cyano-1,10-phenanthroline).[9]

EXPERIMENTAL SECTION

Materials and Instrumentation. All chemicals used in this work were analytical-reagent grade. CH_3CN was freshly distilled over P_4O_{10} for electrochemical measurements. NMR spectra were obtained in CD_3CN with a Bruker 500 MHz equipment, operating at a frequency of 500.13 MHz for ^1H NMR, 125.75 MHz for ^{13}C NMR, and 50.67 MHz for ^{15}N NMR. ESI mass spectra were recorded on a Bruker Esquire 6000 mass spectrometer. Absorption spectra were recorded on a Varian Cary 50 spectrophotometer using 1 cm quartz cells. Emission measurements for Ar-degassed solutions were carried out in 1 cm fluorescence cells with a Shimadzu RF-5301 PC spectrofluorometer at room temperature. Photoluminescence (PL) measurements in the solid state were performed using the 325 and 442 nm lines of a HeCd laser as the excitation radiation. Emission spectra were detected with an Ocean Optics charge-coupled device spectrometer. Measurements were typically performed within a cryostat with samples held at liquid He temperature. Ground state infrared spectra (4000−400 cm^{-1}) were measured as KBr pellets with a Perkin-Elmer FTIR RX-I spectrophotometer. Raman spectra were recorded in the range 3500−350 cm^{-1} on a Raman spectrometer DXR from Thermo Scientific, provided with a trinocular Olimpus Microscope. Electrochemical measurements were carried out using BAS Epsilon EC equipment. A standard three-electrode arrangement was used, with vitreous carbon as working electrode, Pt wire as auxiliary electrode, and Ag/AgCl (3 M KCl) as reference electrode. All solutions were prepared in freshly distilled CH_3CN, with tetra-*n*-butylammonium hexafluorophosphate ($TBAPF_6$) as the supporting electrolyte, and thoroughly degassed with Ar prior to each measurement. Reported $E_{1/2}$ values were calculated as the averages between the peak values corresponding to the cathodic (E_c) and anodic (E_a) waves: $E_{1/2} = (E_c + E_a)/2$. Data obtained by cyclic voltammetry (CV) were almost equal to those obtained by differential pulse voltammetry (DPV). UV−vis spectroelectrochemical experiments were performed in CH_3CN (0.1 M $TBAPF_6$) using a 1 mm path length spectroelectrochemical cell (CH Instruments) with Pt grid as working electrode, Pt wire as counter electrode, and Ag/AgCl (3 M KCl) as reference electrode. Lifetimes and transient spectra of the lowest lying ^{3}MLCT excited states were obtained with a laser flash photolysis setup as described previously.[10,11] Lifetimes were also determined by a time-correlated single photon counting (TCSPC) technique, with Tempro-01 apparatus from Horiba Jobin Yvon (Glasgow, U.K.), using as the excitation pulse source an ultrafast 450(±15) nm Nanoled, operating at 250 kHz. Emission was collected at the emission maximum of complexes **1**−**3** with a monochromator with emission bandwidth selected at 12 nm. Fluorescence intensity decay was fitted with the Fluorescence Decay Analysis Software DAS6 of Horiba Jobin Yvon by deconvolution of the pulse function using a single-exponential model function. All measurements were performed at room temperature in acetonitrile solutions saturated by bubbling for 20 min with high-purity argon, air, and oxygen gases (>99.98, Indura SRL, Argentina). Time-resolved phosphorescence detection of $^1O_2$ was performed with a homemade setup composed by a Peltier-cooled Ge photodiode (Judson J16TE2-66 G, USA) placed at a right angle to the excitation laser pulse. Spurious light was filtered with a 1270 nm band-pass filter (Spectrogon BP-1260). In all cases, transient signals were fed to a Tektronix TDS3032B digital oscilloscope linked to an online PC for data transfer and analysis. Laser energies employed were attenuated so as not to exceed 1.5 mJ per pulse. Individual luminescence traces (20 at least) were signal averaged and fitted by means of a single-exponential function to yield the luminescence intensity I_0 at t = 0. I_0 values were measured at different laser intensities and compared with those obtained from an optically matched solution of perinaphthenone (PN) in CH_3CN as a standard (Φ_Δ = 0.92),[12] thereby yielding relative Φ_Δ values of the Ru(II) complexes. Calculations were obtained using Gaussian '98.[13] Molecules were optimized using Becke's three-parameter hybrid functional B3LYP,[14] with the local term of Lee, Yang, and Parr.[15] Basis set LanL2DZ was chosen for all atoms, and geometry optimizations were performed in the gas phase. No symmetry restrictions were placed on the geometry optimizations. Frequency calculations were performed to ensure that these geometries corresponded to global minima: no imaginary frequencies were obtained for the optimized geometries. The effect of the solvent was included using the polarizable continuum model (PCM) for calculating orbital energy levels and UV−vis spectra in CH_3CN. The contribution of the different groups on the orbitals, calculated UV−vis spectra, and transitions related to them were obtained using the GaussSum Version 2.2 Program.[16] UV−vis profiles were obtained by considering a typical half-bandwidth of $\Delta\nu_{1/2}$ = 3000 cm^{-1} for all electronic transitions.[17,18] Chemical analyses were carried out at INQUIMAE, University of Buenos Aires, Buenos Aires, Argentina, with an estimated error of ±0.5%.

Crystal-Structure Determination. Measurements were carried out on a BRUKER SMART APEX CCD diffractometer using graphite-monochromated Mo Kα radiation (λ = 0.71073 Å) from an X-ray tube. Measurements were made in the range from 2.08° to 28.32° for θ. Full-sphere data collection was carried out with ω and φ scans. A total of 28 138 reflections were collected of which 8649 [R(int) = 0.0566] were unique. The programs used were as follows: data collection, Smart;[19] data reduction, Saint;[20] absorption correction, SADABS.[21] Structure solution and refinement were done using SHELXTL Version 6.14 (Bruker AXS 2000−2003).[22]

The structure was solved by direct methods and refined by full-matrix least-squares methods on F^2. Non-hydrogen atoms were refined anisotropically. H atoms were placed in geometrically optimized positions and forced to ride on the atom to which they are attached. Final R indices [$I = 2\sigma(I)$]: R_1 = 0.0692, wR_2 = 0.1370. R indices (all data): R_1 = 0.1067, wR_2 = 0.1535.

Crystallographic data (excluding structure factors) have been deposited with the Cambridge Crystallographic Data Centre as supplementary publication No. CCDC 831703. Copies of these data can be obtained free of charge on application to CCDC, 12 Union

dx.doi.org/10.1021/ic302594b | Inorg. Chem. 2013, 52, 4950−4962

Road, Cambridge CB2 1EZ, U.K. (fax (44) 1223336-033; E-mail deposit@ccdc.cam.ac.uk).

Syntheses. Ligand 4-methyl-2,2′-bipyridine-4′-carbonitrile (Mebpy-CN) was synthesized following procedures reported in the literature.[23] Precursors $Ru(bpy)_2Cl_2{\cdot}2H_2O$ and $Ru(Mebpy\text{-}CN)_2Cl_2$ were obtained according to a known method.[24]

$([Ru(bpy)_2(Mebpy\text{-}CN)](PF_6)_2$, ***1***. A mixture of 20 mg of Mebpy-CN (0.102 mmol) and 50 mg of $Ru(bpy)_2Cl_2{\cdot}2H_2O$ (0.096 mmol) was added to 50 mL of deaerated CH_3OH and heated at reflux under Ar for 4 h. The obtained reddish-orange solution was rotoevaporated to dryness, redissolved in a minimum amount of water, and passed through a CM Sephadex C-25 column. The complex was eluted with 0.1 M HCl, neutralized with a concentrated solution of KOH, and rotoevaporated to ca. 5 mL. Then, a concentrated aqueous solution of NH_4PF_6 (2 g in 5 mL of water) was added, and the mixture was stored in the refrigerator overnight. The obtained red-orange solid was filtered, washed with water and ether, and stored under vacuum over P_4O_{10} for 1 day. Yield: 55 mg (62%). Chemical analyses and NMR and mass spectra were coherent with the formula $[Ru(bpy)_2(Mebpy\text{-}CN)](PF_6)_2{\cdot}H_2O$. Anal. Calcd (Found) for $C_{32}H_{27}F_{12}N_7OP_2Ru$: C, 41.9 (42.3); H, 3.0 (3.0); N, 10.7 (10.3). ^{1}H NMR (500.13 MHz, CD_3CN): 2.58 (s, 3H), 7.29 (d, 5.5 Hz, 1H), 7.41 (br t, 4H), 7.57 (d, 5.5 Hz, 1H), 7.67 (dd, 1.6 and 5.9 Hz, 1H), 7.74 (br d, 4H), 7.88 (d, 5.9 Hz, 1H), 8.07 (br t, 4H), 8.50 (br d, 4H), 8.57 (s, 1H), 8.82 (d, 1.6 Hz, 1H). ^{13}C NMR (125.75 MHz, CD_3CN): 21.18, 122.75, 125.18, 125.18, 125.20, 125.21, 125.63, 126.46, 128.47, 128.53, 128.53, 128.55, 129.63, 138.78, 138.79, 139.79, 138.83, 142.82, 151.66, 151.76, 152.50, 152.55, 152.60, 152.68, 153.36, 156.90, 157.71, 157.83, 157.90, 157.91, 158.90, 165.80. ^{15}N NMR (50.67 MHz, CD_3CN): 240.6, 259.1, 249.6. Positive ESI MS ion clusters at m/z: 771.9 $\{M - PF_6\}^+$, 313.6 $\{M - 2PF_6\}^{2+}$. IR (KBr pellet, cm^{-1}): 3124(vw), 2925(vw), 2244(vw), 1618(m), 1447(m), 839(vs), 762(s), 557(s). UV–vis (CH_3CN) λ/nm ($\varepsilon \times 10^{-4}/M^{-1}\ cm^{-1}$): 245 (2.2), 286 (6.65), 350 (0.53), 454 (1.2).

$[Ru(bpy)(Mebpy\text{-}CN)_2](PF_6)_2$, ***2***. A mixture of 28 mg of bpy (0.179 mmol) and 100 mg of $Ru(Mebpy\text{-}CN)_2Cl_2$ (0.178 mmol) was added to 50 mL of CH_3OH and heated at reflux for 8 h. A concentrated aqueous solution of NH_4PF_6 (2 g in 5 mL of water) was added, and the obtained red solid was filtered immediately and washed with water and ether. Then it was redissolved in a minimum amount of CH_3OH (ca. 5 mL), filtered, and then precipitated by adding 50 mL of ether. The red-orange solid was filtered after standing overnight in the refrigerator, washed with water and ether, and dried under vacuum over P_4O_{10} for 1 day. Yield: 60 mg (34%). Chemical analyses and NMR and mass spectra were coherent with the formula $[Ru(bpy)(Mebpy\text{-}CN)_2](PF_6)_2{\cdot}3H_2O$. Anal. Calcd (Found) for $C_{34}H_{32}F_{12}N_8P_2O_3Ru$: C, 41.2 (41.4); H, 3.2 (3.4); N, 11.3 (10.9).^{1}H NMR (500.13 MHz, CD_3CN): 2.53 (s, 6H), 7.31 (br, 2H), 7.41 (br, 2H), 7.53 (br, 2H), 7.62 (br, 2H), 7.65 (br, 2H), 7.88 (br, 2H), 8.08 (br, 2H), 8.41 (br, 2H), 8.50 (br, 2H), 8.76 (br, 2H). ^{13}C NMR (125.75 MHz, CD_3CN): 21.0, 116.0, 124.7, 126.4, 126.7, 128.0, 129.1, 129.8, 138.7, 151.2, 151.8, 152.3, 153.6, 155.6, 157.2, 157.3, 159.1. Positive ESI MS ion clusters at m/z: 324.1 $\{M - 2PF_6\}^{2+}$. IR (KBr pellet, cm^{-1}): 3118(w), 2930(vw), 2240(vw), 1620(m), 1448(m), 842(vs), 768(w), 558(s). UV–vis (CH_3CN) λ/nm ($\varepsilon \times 10^{-4}/M^{-1}\ cm^{-1}$): 249 (2.2), 294 (4.3), 370 (0.52), 473 (1.2).

$[Ru(Mebpy\text{-}CN)_3](PF_6)_2$, ***3***. A mixture of 20 mg of Mebpy-CN (0.102 mmol) and 60 mg of $Ru(Mebpy\text{-}CN)_2Cl_2$ (0.106 mmol) was added to 50 mL of CH_3OH and heated at reflux for 10 h. The obtained reddish-orange solution was rotoevaporated to dryness, redissolved in a minimum amount of water, and passed through a CM Sephadex C-25 column. The complex was eluted with 0.1 M HCl, neutralized with a concentrated solution of KOH, and rotoevaporated to ca. 5 mL. Then, a concentrated aqueous solution of NH_4PF_6 (2 g in 5 mL of water) was added, and the mixture was stored in the refrigerator overnight. The red-orange solid was filtered, washed with water and ether, and stored under vacuum over P_4O_{10} for 1 day. Yield: 45 mg (45%). Chemical analyses and NMR and mass spectra were coherent with the formula $[Ru(Mebpy\text{-}CN)_3](PF_6)_2{\cdot}0.5H_2O$. Anal. Calcd (Found) for $C_{36}H_{28}F_{12}N_9O_{0.5}P_2Ru$: C, 43.9 (44.0); H, 2.9 (3.2); N, 12.8 (12.5). ^{1}H NMR (500.13 MHz, CD_3CN): 2.59 (s, 9H), 7.33 (m, 3H), 7.53 (br, 3H), 7.65 (br, 3H), 7.87 (br, 3H), 8.44 (br, 3H), 8.78 (br, 3H). ^{13}C NMR (125.75 MHz, CD_3CN): 21.2, 116.7, 126.9, 127.0, 127.5, 129.4, 130.3, 151.8, 152.6, 154.0, 155.9, 159.7. Positive ESI MS ion clusters at m/z: 343.7 $\{M - 2PF_6\}^{2+}$. IR (KBr pellet, cm^{-1}): 3430(s), 2928(vw), 2240(vw), 1618(m), 1414(w), 842(vs), 770(s), 558(s).UV–vis (CH_3CN) λ/nm ($\varepsilon \times 10^{-4}/M^{-1}\ cm^{-1}$): 248 (2.6), 299 (4.4), 376 (0.53), 471 (1.16).

$[(bpy)_2Ru^{II}(Mebpy\text{-}CN)Ru^{II}(NH_3)_5](PF_6)_4$, ***4***. A solution of 100 mg of **1** (0.109 mmol) in acetone (20 mL) was purged with Ar for 30 min. Then, 50 mg of $[Ru(NH_3)_5(H_2O)](PF_6)_2$ (0.101 mmol), prepared according to a reported method,[25] was added, and the resulting mixture was stirred under Ar for 4 h. The dark-red solution was concentrated to ca. 5 mL, and 50 mL of ether was added to precipitate a dark red solid, which was stored overnight. The solid was filtered, rinsed with ether, and purified by chromatography in alumina (CH_3OH: $(CH_3)_2CO$, 1:1). Unreacted mononuclear precursor eluted first, while the new dinuclear complex was collected afterward, rotoevaporated to ca. 5 mL, precipitated by ether, and stored in the refrigerator overnight. Finally, a dark red solid was filtered. Yield: 24 mg (20%). Chemical analyses and NMR and mass spectra were coherent with the formula $[(bpy)_2Ru(Mebpy\text{-}CN)Ru(NH_3)_5](PF_6)_2{\cdot}3H_2O{\cdot}CH_3OH$. Anal. Calcd (Found) for $C_{33}H_{50}F_{24}N_{12}O_4P_4Ru_2$: C, 27.1 (27.3); H, 3.4 (3.1); N, 11.5 (11.1). ^{1}H NMR (500.13 MHz, CD_3CN): 2.59 (s, 3H), 7.31 (br, 1H), 7.43 (br, 4H), 7.52 (br, 1H), 7,58 (br, 1H), 7.73 (br, 4H), 7.87 (br, 1H), 8.09 (br, 4H), 8.43 (br, 1H), 8.52 (br, 4H), 8.76 (br, 1H). ^{13}C NMR (125.75 MHz, CD_3CN): 20.7, 116.3, 122.1, 124.8, 126.0, 127.0, 128.0, 129.0, 129.2, 138.3, 151.3, 151.3, 152.1, 153.0, 156.0, 157,3, 158.4. Positive ESI MS ion clusters at m/z: 753.8 $\{M - Ru(NH_3)_5(PF_6)_3\}^+$, 313.6 $\{M - 3PF_6\}^{3+}$. IR (KBr pellet, cm^{-1}): 3368(s), 2928(vw), 2181(s), 1605(m), 1447(w), 1288(w), 840(vs), 763(s), 558(s). UV–vis (CH_3CN) λ/nm ($\varepsilon \times 10^{-4}/M^{-1}\ cm^{-1}$): 252 (2.9), 287 (5.5), 340 (0.71), 449 (1.3), 518 (1.9).

$[(bpy)_2Ru^{II}(Mebpy\text{-}CN)Ru^{III}(NH_3)_5]^{5+}$, ***5***. **5** was prepared in situ by oxidizing **4** with an excess of $Br_2(g)$ in CH_3CN solution.

Preparation of ZnO Nanowires. ZnO nanowires (NW) growth was performed on the LAFISO vapor-transport system, which consists of a quartz tube placed within a tubular furnace whose one side is seal connected through a vacuum valve to a rotary pump while the other side to high purity (99.999%) Ar and O_2 lines.[26] An alumina crucible containing mixed ZnO and graphite powders (1:1 weight ratio) was placed inside the quartz tube at a position corresponding to the furnace center. Substrates were amorphous SiO_2 layers (0.5 μm thick, grown on Si by thermal oxidation) where a thin (5 nm) Au layer had been deposited and annealed at 500 °C for 15 min to produce nanometer-sized Au clusters on it. Such a SiO_2/Si substrate piece was placed parallel to the tube axis facing upward at a distance of 15.7 cm from the furnace center downstream the tube. After Ar purging and evacuating the quartz tube to ~20 mTorr, steady Ar and O_2 flows were established by graduated valves, raising the pressure in the tube to slightly above 1 Torr. The furnace temperature at its center was then ramped to T_{crus} = 1100 °C at 25 °C/min, maintained constant at 1100 °C for 1 h, and then naturally cooled down to room temperature.

Figure S1 (Supporting Information) shows a top view of the sample morphology, obtained by scanning electron microscopy (SEM). It mainly consists of a dense network of well-defined ZnO NWs of about 10 μm in length and a wide width distribution (mean of about 250 nm) and some nanosheets. The used equipment was a Carl Zeiss SUPRA-55 scanning electron microscope from CIME (UNT-CONICET) with a resolution of 1.0 nm at 15 kV and 1.7 nm at 1 kV in high-vacuum (HV) mode and 2 nm at 30 kV in variable-pressure mode (VP). A piece of the sample was soaked in complex **1** for ~30 days to allow the Ru complex to penetrate deep into the void regions between NWs. The electrical photocurrent spectrum of the NW network with and without the Ru complex, was determined by applying a dc bias (100 V) between two Al/Au ohmic contacts Ar sputtered on the top of the network (separation of ~1 mm) and measuring the current during monochromatic illumination in the 250–1100 nm range. A 500W Xe lamp coupled to a monochromator by collimating lenses was used as a light source. Second-order

dx.doi.org/10.1021/ic302594b | Inorg. Chem. 2013, 52, 4950–4962

reflections from the monochromator gratings were cut with color filters.

RESULTS AND DISCUSSION

Syntheses and IR and NMR Spectra. The synthetic procedures are similar to those previously described for related polypyridyl ruthenium(II) complexes,[9] with chromatographic separations taking into account the higher basicity of the Mebpy-CN ligand as compared to bpy. IR spectra of complexes **1**−**4** exhibit the typical vibrational modes of the polypyridyl ligands (bpy and Mebpy-CN) between 1650 and 1400 cm^{-1} and the characteristic band corresponding a C≡N stretching mode, ν(C≡N). As shown in Figure 1, the IR spectrum of **1**

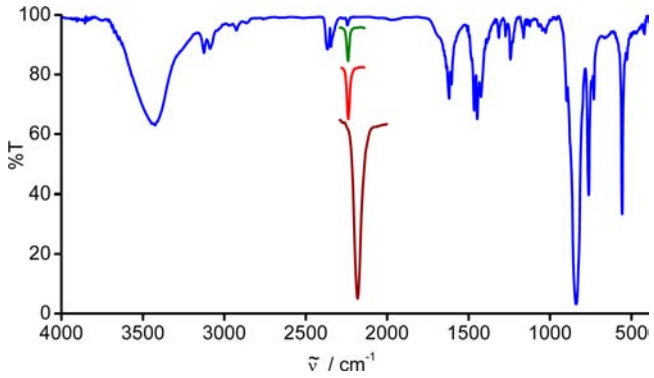

Figure 1. IR spectrum of **1** (blue line). (Inset) CN stretching bands of **2** (green line), **3** (red line), and **4** (wine-red line) are shown at the same scale (KBr pellets).

has a low-intensity band at ν(C≡N) = 2244 cm^{-1}, which is displaced 10 cm^{-1} to higher wavenumbers with respect to that of the free ligand, consistent with the C≡N bond length determined by X-ray diffraction studies (vide infra). The corresponding value observed in the related complex [Ru(bpy)$_2$(5-CNphen)](PF$_6$)$_2$·H$_2$O (5-CNphen = 5-cyano-1,10-phenanthroline), previously described in our group, ν(C≡N) = 2231 cm^{-1}, is also displaced at higher frequencies when compared to the free ligand value ($\Delta\nu$ = 9 cm^{-1}).[9] These small shifts can both be attributed to metal coordination to the pyridine nitrogens of Mebpy-CN. As expected, the intensity of the nitrile stretching band increases in the series [Ru(bpy)$_{3-x}$(Mebpy-CN)$_x$](PF$_6$)$_2$ when going from x =1 to x = 3 (see Figure 1), with almost no change in frequency. In contrast, complex **4** displays a very intense nitrile stretching band at ν(C≡N) = 2181 cm^{-1}, also shown in Figure 1, considerably shifted to a lower value than that of the free ligand ($\Delta\nu$ = −58 cm^{-1}) as a consequence of the strong π-backbonding effect from d_π orbitals of ammine Ru to π^* orbitals of the nitrile moiety of Mebpy-CN. Complex **4** also displays the characteristic ammonia symmetric deformation mode δ_{sym}(NH$_3$) = 1288 cm^{-1}, a clear indication of oxidation state (II) for the ammine ruthenium.[9]

The ^{1}H NMR spectrum of **1** in CD$_3$CN shows a remarkable signal corresponding to the H bonded to the adjacent carbon of the nitrile group (8.82 ppm) due to the strong deshielding effect of this moiety. The same effect is reproduced in complexes **2**−**4**. ^{13}C NMR shifts indicate that the bipyridines are inequivalent in the whole series. Complete assignment of all signals of complex **1** is shown in Figure S2 (Supporting Information). Equivalent procedures were carried out for complexes **2**−**4**, although the multiplicities are not clearly seen for these species, probably because of their inherent asymmetries and/or the coexistence of stereoisomers with equivalent physicochemical properties. The stereochemistry in octahedral metal complexes with bidentate ligands has already been analyzed in detail by Keene.[27] The possible existence of geometric isomers has also been acknowledged in similar complexes, although no evidence of differences in their characteristics have been determined; it is therefore assumed that spectroscopic, electrochemical, and photophysical data represent an average of the various forms.

Crystal Structure. The crystal structure of complex **1** was solved by X-ray diffraction analysis. Crystals were obtained by slow diffusion of ether onto a concentrated solution of the complex in acetonitrile. Figure 2 displays the molecular

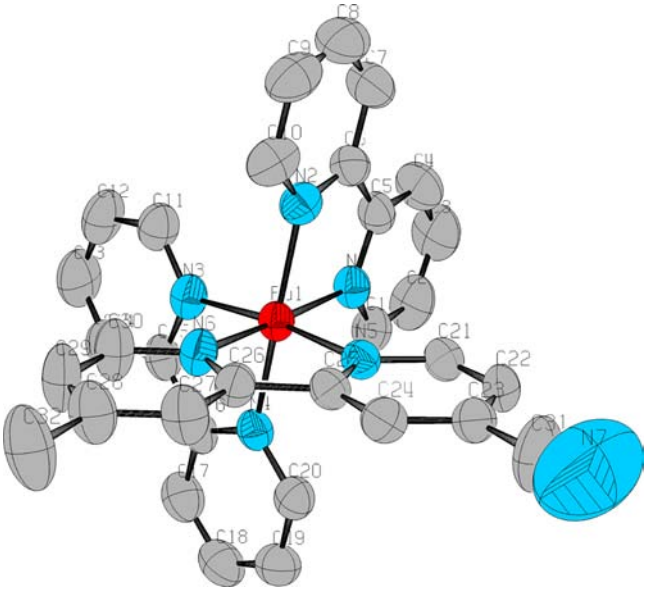

Figure 2. ORTEP diagram[30] (ellipsoids at 70% probability) of [Ru(bpy)$_2$(Mebpy-CN)]$^{2+}$ with C atoms in black, N atoms in blue, and Ru atom in red. All H atoms have been omitted for clarity.

structure of the cation of **1**, whereas the main crystallographic data and selected bond distances and angles can be found in Tables 1 and 2, respectively. The structure is that of a slightly distorted octahedron. All bond distances and angles are within the expected values for Ru bipyridyl complexes; for example, the Ru−N(py) mean distance in related complexes is 2.058 Å.[28] However, it is interesting to note that the Ru−N5 bond length, where the pyridyl ring contains the nitrile group, is slightly longer (2.071 Å) than the distance found for Ru−N6 (2.061 Å), where the pyridyl ring contains the CH_3 group, thus evidencing the stronger electron-withdrawing character of the CN substituent with respect to the CH_3 substituent. The N−Ru(1)−N angles around 78° show the geometrical restrictions imposed by the bidentate pyridyl ligands; consequently, the rest of the equatorial angles are larger than 90° expected for an ideal octahedral geometry. Finally, The distance C≡N (1.01 Å) is shorter than the characteristic distance of a nitrile bounded at an aromatic group,[29] which can be attributed to remote metal coordination.

UV−Vis Spectra. The UV−visible spectrum of **1** in CH_3CN, displayed in Figure 3, shows a characteristic metal-to-ligand charge-transfer (MLCT) band centered at λ_{max} = 454 nm, a π−π^* transition at λ_{max} = 245 nm, metal-centered (MC)

dx.doi.org/10.1021/ic302594b | Inorg. Chem. 2013, 52, 4950−4962

Table 1. Crystallographic Data for Complex 1[a]

empirical formula	$C_{31}H_{25}F_{12}N_7P_2Ru$
fw	898.60
cryst syst	triclinic
space group	*P*-1
a [Å]	11.023(2)
b [Å]	12.207(3)
c [Å]	14.157(3)
α [deg]	97.740(4)
β [deg]	98.339(4)
γ [deg]	105.093(4)
V [Å^3]	1789.9(7)
formula units/cell	2
temp, K	300(2)
ρ_{calcd}, [Mg/m^{-3}]	1.667
μ[mm^{-1}]	0.626
final *R* indices, [$I > 2\sigma(I)$]	$R_1 = 0.0692$
	$wR_2 = 0.1370$
R indices [all data]	$R_1 = 0.1067$
	$wR_2 = 0.1535$

[a] $R_1 = \Sigma||F_o| - |F_c||/\Sigma|F_o|$. $wR_2 = [\Sigma\{w(F_o^2 - F_c^2)^2\}/\Sigma\{w(F_o^2)^2\}]^{1/2}$, where $w = 1/[\sigma^2(F_o^2) + (0.0042P)^2]$ and $P = (F_o^2 + 2F_c^2)$.

Table 2. Selected Bond Lengths (Angstroms) and Angles (degrees) for Complex 1

Ru(1)–N(4)	2.057(4)
Ru(1)–N(3)	2.061(4)
Ru(1)–N(6)	2.061(4)
Ru(1)–N(2)	2.063(4)
Ru(1)–N(1)	2.065(4)
Ru(1)–N(5)	2.071(4)
N(4)–Ru(1)–N(3)	78.76(17)
N(4)–Ru(1)–N(6)	88.27(15)
N(3)–Ru(1)–N(6)	95.43(14)
N(4)–Ru(1)–N(2)	173.25(15)
N(3)–Ru(1)–N(2)	97.50(16)
N(6)–Ru(1)–N(2)	97.73(16)
N(4)–Ru(1)–N(1)	95.50(15)
N(3)–Ru(1)–N(1)	87.07(14)
N(6)–Ru(1)–N(1)	175.83(16)
N(2)–Ru(1)–N(1)	78.61(16)
N(4)–Ru(1)–N(5)	96.5915)
N(3-Ru(1)–N(5)	172.43(15)
N(6)–Ru(1)–N(5)	78.35(14)
N(2)–Ru(1)–N(5)	87.70(15)
N(1)–Ru(1)–N(5)	99.39(14)

bands at λ_{max} ca. 320 and 350 nm, and a ligand-centered (LC) band at λ_{max} = 286 nm. These assignments were made by comparison to the bands of $[Ru(bpy)_3]^{2+}$, also shown in Figure 3. In this reference complex, the bands detected at λ_{max} = 450 and 240 nm (with the first one with a shoulder near 400 nm) have been assigned to three different $d_\pi(Ru) \rightarrow \pi^*$ (bpy) transitions.[31] The lowest lying MLCT band of **1** is slightly shifted to a longer wavelength than that of the reference complex, as expected by the presence of a strongly electron-accepting nitrile group (CN) in the 4′ position of one of the bipyridine ligands, partially compensated by the presence of an electron donor methyl group (CH_3) in the 4 position of the same ligand. When increasing the substitution of bpy by Mebpy-CN, the energy of the lowest lying MLCT decreases; in effect, complex **2** absorbs at λ_{max} = 473 nm, while complex **3**

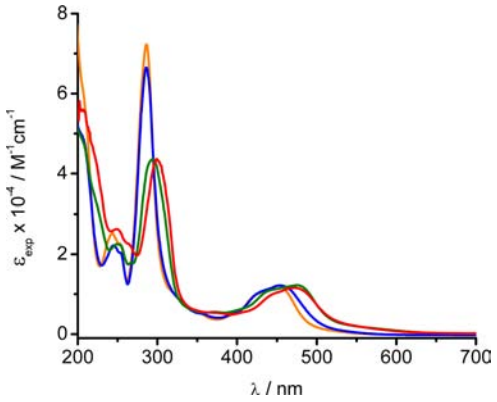

Figure 3. UV–vis spectra of **1** (blue line), **2** (green line), **3** (red line), and $[Ru(bpy)_3]^{2+}$ (orange line) in CH_3CN.

absorbs at λ_{max} = 471 nm, as shown in Figure 3. These shifts can be related to the electron-withdrawing effect of the nitrile group in Mebpy-CN, which causes a decrease in energies of the LUMOs when going from **1** to **3**, as confirmed by computational calculations (vide infra). The increase of electronic delocalization induced by increasing the number of nitrile groups produces a decrease of the energy of the first MLCT and IL band of complexes **1**–**3**. These findings are consistent with the observations of McCusker et al. in related complexes;[8] for example, MLCT transitions associated with the ligand CN-Me-bpy in $[Ru(bpy)_2(CN\text{-}Me\text{-}bpy)]^{2+}$ appear at lower energies than the corresponding transitions coupled to the unsubstituted bpy ligands. The appearance of the MLCT absorption at a slightly higher energy in **3** than in **2** can be adscribed to its higher symmetry.[8]

The UV–vis spectrum of complex **4** is shown in Figure 4 (together with that of $[Ru(bpy)_3]^{2+}$ for comparison purposes):

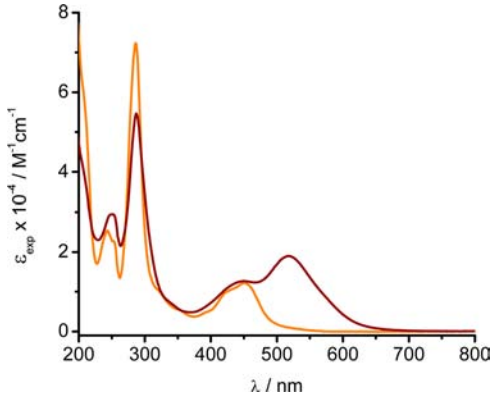

Figure 4. UV–vis spectra of **4** (wine-red line) and $[Ru(bpy)_3]^{2+}$ (orange line) in CH_3CN.

two different MLCT bands appear at λ_{max} = 518 and 449 nm, corresponding to the pentaammine ruthenium (Ru_a) to Mebpy-CN charge transfer and the bipyridyl ruthenium (Ru_b) to Mebpy-CN charge transfer, respectively. These assignments are confirmed by spectroelectrochemical experiments and the results of the calculations of the UV–vis spectra by TD-DFT (vide infra).

Electrochemistry and Spectroelectrochemistry. Redox potentials obtained from cyclic voltammograms of complexes **1**–**4** in CH_3CN with 0.1 M $TBAPF_6$, vs SCE are shown in Table 3. Increasing substitution of bpy by Mebpy-CN increases

dx.doi.org/10.1021/ic302594b | Inorg. Chem. 2013, 52, 4950–4962

Table 3. Electrochemical Data for complexes 1−4 in CH_3CN vs SCE

complex	$E_{1/2}^{ox}$, V	$E_{1/2}^{red1}$, V	$E_{1/2}^{red2}$, V	$E_{1/2}^{red3}$, V	$\Delta E_{1/2}$,[a] V	$10^{-4}\ \nu_{MLCT}$, cm^{-1}
1	1.28	−1.36	−1.57	−1.78	2.64	2.20
2	1.41	−1.02	−1.22	−1.65	2.43	2.11
3	1.45	−1.01	−1.17	−1.38	2.46	2.12
4	1.34, 0.64	−1.16	−1.50	−1.76	2.50,1.80	2.22, 1.93

[a] $\Delta E_{1/2} = (E_{1/2}^{ox} - E_{1/2}^{red1})$.

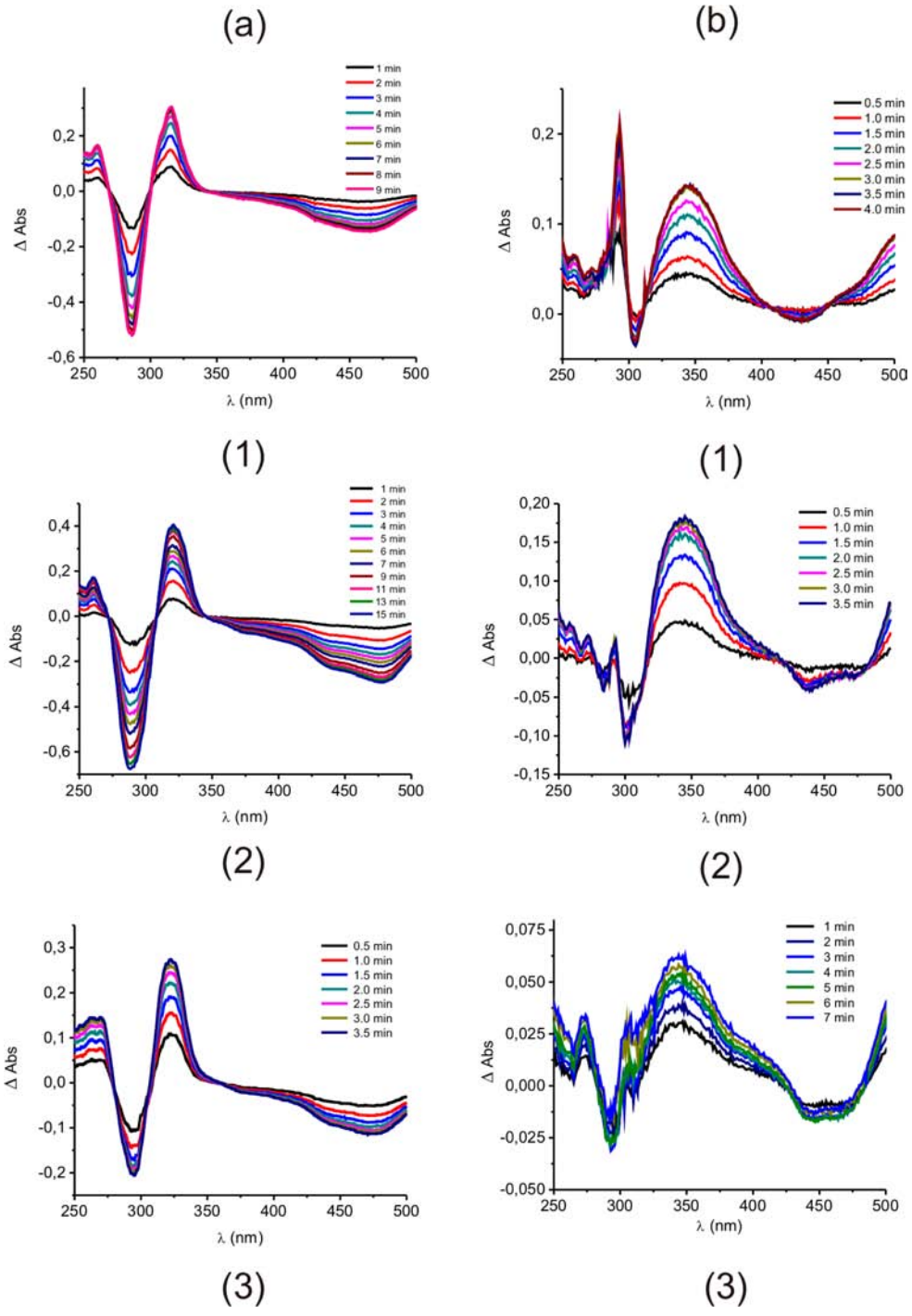

Figure 5. (a) Oxidative difference spectra acquired at an applied potential 150 mV higher than the oxidation potential of the metallic center of **1**, **2**, and **3**, from top to bottom, respectively. (b) Reductive difference spectra acquired at an applied potential 75 mV lower than the first reduction potential of **1**, **2**, and **3**, from top to bottom, respectively.

dx.doi.org/10.1021/ic302594b | *Inorg. Chem.* 2013, 52, 4950−4962

both the oxidation potential of the metallic center and the reduction potentials of the ligands. The first effect is related to the strong electron-withdrawing effect of the nitrile substituent which stabilizes oxidation state II for ruthenium. The last effect is related to stabilization of Mebpy-CN, as compared to bpy, due a higher electronic delocalization in the aromatic ring induced by the nitrile group. There is a correspondence between the electrochemical data and the positions of the MLCT bands. In effect, there is a linear relationship between $\Delta E_{1/2} = E_{1/2}^{ox} - E_{1/2}^{red1}$ and the maximum frequency of the MLCT bands ν_{MLCT} (see Table 3), as observed before in other mixed-ligand ruthenium bipyridyl complexes.[32] All electrochemical waves are quasi-reversible and typical of bipyridyl ruthenium complexes. Complex **3** presents an irreversible fourth reduction wave at $E_{1/2} = -1.65$ V, as determined by DPV.

The dimetallic complex **4** has a higher oxidation potential for the bipyridyl ruthenium couple than that of **1**, as expected when considering its higher charge. The oxidation potential of the pentaammine ruthenium couple (0.64 V) is a typical value expected for a nitrile-coordinated species.[9]

Spectroelectrochemical studies were carried out on complexes **1**−**3**, confirming the nature of the oxidized and reduced species and consequently assignment of the potential redox potentials of the voltamogramms. In effect, as shown in Figure 5, the MLCT band disappears when oxidizing the ruthenium center and a new LF band appears at 330 nm, while new bands appear at 350 and 370 nm when reducing Mebpy-CN, which are typical of bpy radicals.[8] These data will be used later to explain spectroscopic data of transient species obtained by visible light excitation. All studied complexes exhibited almost complete recovery of initial spectra when reoxidized or rereduced.

Photophysical Properties. Relative radiative quantum yields were calculated using eq 1

$$\Phi_x = \Phi_r[(I_x/A_x)/(I_r/A_r)](\eta_x/\eta_r)^2 \quad (1)$$

where Φ_r is a quantum yield of a reference ($[Ru(bpy)_3](PF_6)_2$ in acetonitrile, $\Phi_r = 0.095$),[33] I_r and I_x are the integrated sum of the emission intensity of the reference and the sample respectively, A_x and A_r are the absorbances of the sample and the reference at their excitation wavelengths, and η_x and η_r are the refraction indexes of the respective solvents (taken to be equal to the neat solvents).

The photophysical properties of complexes **1**−**3** in CH_3CN at room temperature are summarized in Table 4. They all exhibit higher emission quantum yields and higher lifetimes of the lowest ^{3}MLCT excited states than those of $[Ru(bpy)_3](PF_6)_2$, measured at the same conditions ($\phi_{em} = 0.095$ and $\tau = 0.66$ μs, respectively). Both values (ϕ_{em} and τ) increase with increasing substitutions of bpy by Mebpy-CN, indicating a higher delocalization induced by the nitrile groups, as described before by McCusker et al.[8] The correlation between luminescence yields and emission lifetimes has already been reported in a different series of ruthenium(II) polypyridyl complexes.[34] Figure S3 (Supporting Information) shows the emission spectra of complexes **1**−**4** and $[Ru(bpy)_3]^{2+}$ in CH_3CN at room temperature ($\lambda_{ex} = 450$ nm).

Time-resolved differential absorption spectra of complexes **1**−**3** (Figure 6), obtained by LFP, exhibit the typical bleaching of the MLCT band at $\lambda_{max} = 450$−470 nm. In all cases, new bands appear at 370 nm, associated to IL transitions of the Mebpy-CN radical, and at 330 nm, associated to IL bands of the neutral ligands. Spectroelectrochemical measurements described above confirm these assignments: one band appears

Table 4. Photophysical Properties of Complexes 1−3 in CH_3CN at Room Temperature

complex	λ_{em} (nm)	ϕ_{em}	$\tau/\mu s^a$	$k_{obs}\times 10^{-5}/s^{-1}$	$k_r\times 10^{-5}/s^{-1}$ [b]	$k_{nr}\times 10^{-5}/s^{-1}$ [c]
1	623	0.120	0.76 (0.73)	13.2	1.58	11.6
2	660	0.125	0.97 (1.09)	10.3	1.28	9.0
3	658	0.133	1.16 (1.22)	8.6	1.14	7.5

[a]Data obtained by LFP (in parentheses, data obtained by TCSPC). [b]$k_r = \phi^{em}.k_{obs}$. [c]$k_{nr} = k_{obs} - k_r$.

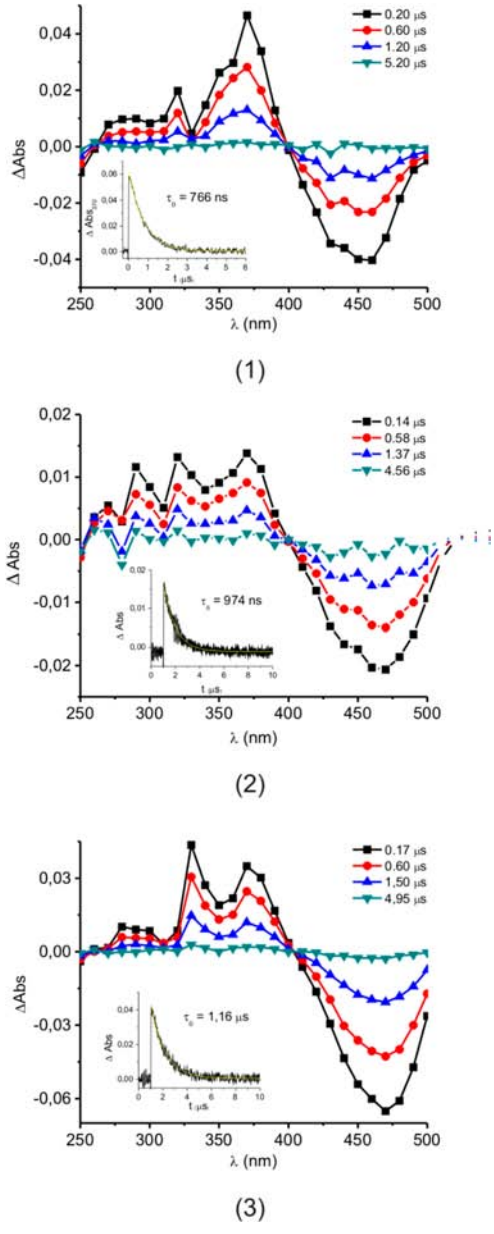

Figure 6. Time-resolved differential absorption spectra of **1** (top), **2** (middle), and **3** (bottom) in CH_3CN at different times (0.14−5.20 μs), $\lambda_{exc} = 370$ nm, obtained by LFP. (Inset) Absorbance decay at 370 nm and monoexponential fitting.

dx.doi.org/10.1021/ic302594b | Inorg. Chem. 2013, 52, 4950−4962

at 350 nm when the complexes are reduced, and a new band at 330 nm appears when the complexes are oxidized, both of them associated to IL transitions. The lowest lying MLCT excited state can thus be formulated as a charge-separated excited state $[Ru^{III}-(Mebpy\text{-}CN\cdot^{-})]$in all complexes. The room-temperature emission spectra (see Figure S3, Supporting Information) do not show vibrational fine structure, as usually expected for molecules of this type. Besides, the wavelengths for maximum emission correlate with the wavelengths for maximum absorption. There are small differences between the values of k_{nr}, and they are similar to that of $[Ru(bpy)_3]^{2+}$ ($k_{nr} = 9.53 \times 10^5\ s^{-1}$), in contrast to the higher variations observed in the series $[Ru(bpy)_{3-n}(CN\text{-}Me\text{-}bpy)_n](PF_6)_2$ ($n = 1-3$),[8] which can be attributed to the effect of having less cyano substituents attached to the pyridyl rings in the present study. Cyano groups are very useful for monitoring electron transfer reactions, because of the strong dependence of its IR frequency on the oxidation state of the metal to which it is connected, as we demonstrated above when analyzing the ground state of the dinuclear species **4**. These shifts are also useful tools to characterize the nature of the chemical bonds in excited states by nanosecond step-scan IR spectroscopy.[8]

As shown in Figure S3, Supporting Information, complex **4** emits at $\lambda_{em} = 650$ nm with a very low quantum yield ($\phi = 0.005$), possibly due to an autoquenching process (the lowest lying MLCT absorption band appears at $\lambda_{max} = 518$ nm). The mixed-valent species **5**, on the other hand, emits at $\lambda_{em} = 630$ nm with quantum yield $\phi = 0.018$, which is almost 6 times less than that of the mononuclear species **1**. This decrease can be attributed to an intramolecular electron transfer process that takes place after light excitation,[9] as shown in Scheme 1, where

Scheme 1. Decay of a MLCT Excited State Through a MMCT Excited State in 5

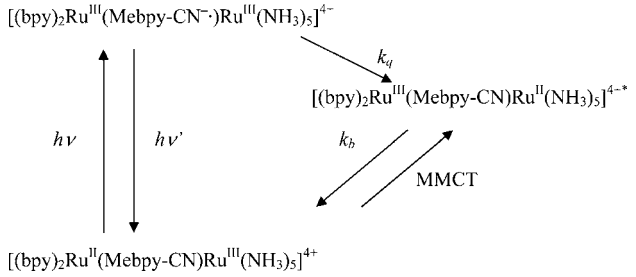

$h\nu$ is the excitation photon, $h\nu'$ is the emissive photon, k_q is the first-order rate quenching constant, k_b is the backward charge recombination process, and MMCT is the absorption process corresponding to a metal-to-metal charge transfer (the "intervalence" transition), which will be described below.

Photosensitization of Singlet Molecular Oxygen, $^1O_2$. Interaction of the ^{3}MLCT excited state by ground state triplet molecular oxygen ($^3O_2$) was also studied. The dependence of the observed pseudo-first-order rate constant, k_{obs} (of both the luminescence decay at the emission maximum and the transient absorption decay at 370 nm of the complexes determined by TCSPC and LFP), with $^3O_2$ concentration is given by eq 2

$$k_{obs} = k_0 + k_q[^3O_2] \quad (2)$$

where $k_0 = 1/\tau_0$ is the intrinsic first-order decay constant of the ^{3}MLCT state in the absence of $^3O_2$. Table 5 collects the quenching rate constant values by molecular oxygen for

Table 5. Rate Constants for Luminescence Quenching of the ^{3}MLCT States of Complexes 1−3 by Molecular Oxygen (k_q), Singlet Oxygen Quantum Yield (Φ_Δ), Fraction of ^{3}MLCT States Quenched by Molecular Oxygen (P_{MLCT}^{O2}), and Efficiency of Singlet Oxygen Production from the ^{3}MLCT State (f_Δ^{MLCT}) in Air-Equilibrated CH_3CN Solutions at 25 °C

complex	$k_q \times 10^{-9}$, $M^{-1}\ s^{-1}$	Φ_Δ[a]	P_{MLCT}^{O2}	f_Δ	$^1k_q \times 10^{-9}$, $M^{-1}\ s^{-1}$	$^3k_q \times 10^{-9}$, $M^{-1}\ s^{-1}$	$^1k_q/^3k_q$
1	1.84	0.53	0.72	0.73	1.35	0.49	2.75
2	1.38	0.42	0.72	0.57	0.78	0.59	1.32
3	1.16	0.40	0.72	0.55	0.64	0.52	1.23

[a]Calculated by actinometry with periphthenone (PN) using $\Phi_\Delta^{PN} = 0.92$

complexes **1**−**3**, k_q, obtained as the slope of the plot of k_{obs} vs $[^3O_2]$, as shown in Figure S4 (Supporting Information) for complex **2**.

The calculated k_q values of all complexes are less by 1 order of magnitude than the expected diffusion-controlled rate constant in CH_3CN, e.g., $k_{dif} = 2.8 \times 10^{10}\ M^{-1}\ s^{-1}$.[35] In turn, k_q values for the Mebpy-CN-substituted complexes are smaller than that for the parent complex $[Ru(bpy)_3]^{2+}$, e.g., $k_q = 1.96 \times 10^9\ M^{-1}\ s^{-1}$, as previously observed by Abdel-Shafi et al. for a series of (substituted 2,2′-bipyridine)ruthenium(II) complexes also in CH_3CN.[35]

In order to probe the generation of $^1O_2$ in the quenching reaction of the ^{3}MLCT excited state of complexes **1**−**3** with $^3O_2$, time-resolved near-infrared phosphorescence detection of $^1O_2$ at 1270 nm experiments were performed in air-saturated CH_3CN solutions. Figure 7 shows the typical transient

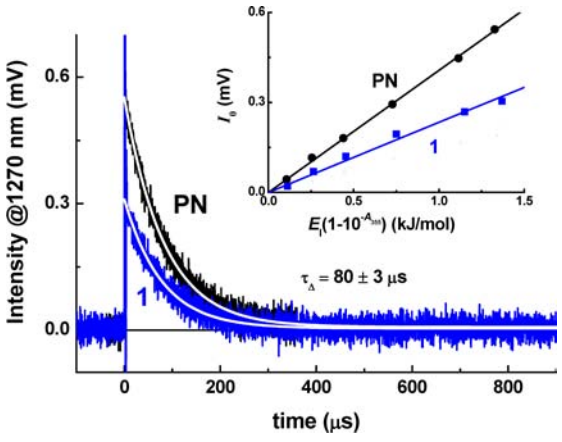

Figure 7. Phosphorescence decays of $^1O_2$ at 1270 nm observed by photosensitization at 355 nm of both the reference PN (50 μM) and complex **1** (80 μM) in aerated CH_3CN solutions together with exponential fitting of the decay portion (white lines). (Inset_ Dependence of the initial intensity of the $^1O_2$ signal as a function of the absorbed excitation energy.

phosphorescence signal of $^1O_2$ at 1270 nm generated after 355 nm laser excitation of both the actinometer perinaphthenone (PN) and **1** in air-saturated CH_3CN solutions. The decay time of $^1O_2$ obtained by photosensitization of both PN and the complexes was coincident with that expected for CH_3CN ($\tau_\Delta \approx 80\ \mu s$), indicating that quenching of $^1O_2$ by the

dx.doi.org/10.1021/ic302594b | Inorg. Chem. 2013, 52, 4950−4962

complexes does not occur within the complex concentrations used (60−80 μM).

The quantum yield of formation of $^1O_2$ (Φ_Δ) by complexes **1**−**3** and also by $[Ru(bpy)_3]^{2+}$ were determined by laser actinometry using the reference compound perinaphthenone (PN). The Φ_Δ values reported in Table 5 demonstrate that complexes **1**−**3** are more efficient photosensitizers for $^1O_2$ than the parent complex $[Ru(bpy)_3]^{2+}$ (Φ_Δ = 0.33), in particular complex 1. Since both the lifetime of the ^{3}MLCT state (τ) and the rate quenching constant by molecular oxygen (k_q) are changing in the complex series, we calculated f_Δ, which is the fraction of ^{3}MLCT states quenched by $^3O_2$ that yield $^1O_2$, using eq 3

$$\Phi_\Delta = \Phi_T P_{O_2} f_\Delta \tag{3}$$

where Φ_T is the population of the lowest excited ^{3}MLCT state, which is considered unity for $[Ru(bpy)_3]^{2+}$ and derivatives,[31,36] and P_{o_2} is the fraction of the ^{3}MLCT states quenched by oxygen, which is given by eq 4

$$P_{O_2} = \frac{k_q[^3O_2]}{k_0 + k_q[^3O_2]} \tag{4}$$

The values of P_{o_2} and f_Δ are listed in Table 5; while P_{o_2} remains constant, f_Δ decreases in the order **1** > **2** > **3** > $[Ru(bpy)_3]^{2+}$. These results are relevant for applications in photodynamic therapy.[34]

The observed quenching rate constant k_q decreases linearly with the oxidation potential $E_{1/2}{}^{Ox}$ of the metallic center (Table 3), indicating charge-transfer control in the quenching reaction. The mechanism of quenching by oxygen of the triplet states of organic molecules has been extensively revised by Wilkinson[37] on the basis of the importance of spin statistical factors introduced by Gijzeman et al.[38] Recently, this mechanism was applied to explain the quenching of the excited ^{3}MLCT state of Ru(II) bipyridine complexes by $^3O_2$ in aqueous solutions.[39] In this mechanism, excited encounter complexes with multiplicities m = 1, 3, and 5 are formed in the primary step of quenching, with diffusion-controlled rate constant k_{dif}, eqs 5−7[35,36]

$$\begin{aligned} {}^3\text{MLCT} + {}^3O_2 &\underset{k_{dif}}{\overset{1/9k_{dif}}{\rightleftharpoons}} {}^1({}^3\text{MLCT}\cdot\cdot{}^3O_2)^* \\ &\xrightarrow{k_{et}} {}^1(\text{MLCT}^+\cdot\cdot O_2^-) \\ &\rightarrow \text{MLCT} + {}^1O_2 \end{aligned} \tag{5}$$

$$\begin{aligned} {}^3\text{MLCT} + {}^3O_2 &\underset{k_{dif}}{\overset{3/9k_{dif}}{\rightleftharpoons}} {}^3({}^3\text{MLCT}\cdot\cdot{}^3O_2)^* \\ &\xrightarrow{k_{isc}} {}^3(\text{MLCT}^+\cdot\cdot O_2^-) \\ &\rightarrow \text{MLCT} + {}^3O_2 \end{aligned} \tag{6}$$

$$ {}^3\text{MLCT} + {}^3O_2 \underset{k_{dif}}{\overset{5/9k_{dif}}{\rightleftharpoons}} {}^5({}^3\text{MLCT}\cdot\cdot{}^3O_2) \tag{7}$$

According to these reactions, $^1O_2$ is only formed through the singlet (m = 1) encounter complex with a spin statistical factor of 1/9 while the triplet (m = 3) encounter complex deactivates the excited ^{3}MLCT state without generating $^1O_2$. The quintet (m = 5) complex has no direct product channel. The fact that $k_q < k_{dif}/9$ could be attributed to an important enhanced intersystem crossing between singlet and triplet charge-transfer intermediate states or even of the enhancement of reaction 6. It has been suggested that the presence of the heavy ion Ru (II) would enhance spin-forbidden pathways,[10] contributing to a k_q value lower than the statistically expected one.

Another fact of this mechanism is that the observed quenching rate constant $k_q = {}^1k_q + {}^3k_q$, where ${}^1k_q$ and ${}^3k_q$ are the quenching rate constant through the singlet and triplet channels, respectively. These quenching rate constants are related with f_Δ by

$${}^1k_q = k_q f_\Delta \tag{8}$$

$${}^3k_q = k_q(1 - f_\Delta) \tag{9}$$

The calculated values of ${}^1k_q$ and ${}^3k_q$ for complexes **1**−**3**, shown in Table 5, indicate that only the singlet channel was decreasing with $E_{1/2}{}^{Ox}$ of the complexes, supporting the assumption that the redox properties of complexes **1**−**3** modulate the photosensitized generation of $^1O_2$.

Sensitization of ZnO Nanowires. It is well known that the photoelectrical (both photocurrent buildup and recovery) response in ZnO is usually very long.[26,40] As a result, the photocurrent does not reach stationary values even after illuminating the sample for times up to ~20 h. Therefore, for the photocurrent measurements, the following procedure was employed. After leaving the sample in the dark for at least 3 days, it was subjected to illumination from 1100 to 250 nm. The wavelength (λ) scan was computer controlled at preset wavelength step (10 nm) and dwell time at each step (60 s). This exact procedure was then repeated for the Ru complex-soaked sample. No photocurrent response was detected for illumination between 1100 and 700 nm in either sample. Figure S5 (Supporting Information) shows the photocurrent measured on the bare and Ru complex-soaked ZnO samples for λ < 700 nm. Spectra have been normalized to their maximum photocurrent value to facilitate comparison of their spectral shape. Photocurrent increases with decreasing λ for both samples, however in a steeper way for the soaked sample. When reaching 400 nm, the photocurrent starts increasing more steeply for both samples with decreasing λ, as a result of photon absorption in the ZnO NWs. An overall comparison of both spectra clearly reveals an extra photocurrent for the Ru complex-soaked sample, indicating a contribution from photon absorption in complex **1** in this range. Figure 8 shows the difference between the photocurrent measured on the Ru

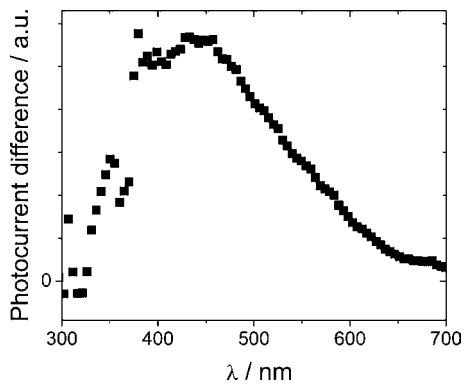

Figure 8. Photoconductivity difference between ZnO nanowires which have been previously soaked with complex **1** and bare ZnO nanowires vs wavelength.

dx.doi.org/10.1021/ic302594b | Inorg. Chem. 2013, 52, 4950−4962

complex-soaked ZnO samples and that measured on the bare ZnO NWs as a function of wavelength in the range λ = 300−700 nm. The measured photocurrent difference has a maximum at $\lambda_{max} \approx$ 450 nm, which is almost coincident with the wavelength for maximum absorption of complex **1** in CH_3CN (λ_{max} = 454 nm), thus evidencing that the observed photocurrent enhancement is due to the sensitizer.

It must be noted that Wang and co-workers recently reported a DSSC with a photoconversion efficiency of 1.18% using ZnO nanotubes as a photoanode sensitized with a Ru(II) complex,[41] while ZnO nanocrystals sensitized with a ruthenium dye that does not aggregate can reach a solar-to-electrical conversion efficiency as high as 4%.[42] Sensitization of ZnO can be accomplished by diffusion of the dye into the ZnO nanostructure, adsorption of the dye to the ZnO surface, or formation of Zn/dye complexes in the pores of the ZnO film. In this study, we propose anchoring of the dye to the ZnO surface through a nitrile group. In effect, as shown in Figure S6 (Supporting Information), when comparing the nitrile stretching frequency, obtained by Raman spectroscopy, of **1** adsorbed onto ZnO nanowires (ν(C≡N) = 2245 cm^{-1}) with that of **1** (ν(C≡N) = 2240 cm^{-1}), a positive shift of 5 cm^{-1} is disclosed, indicating coordination of a nitrile group to a metallic center with no π-back-bonding ability. For example, the nitrile stretching frequency of 2-cyanopyridine is shifted 5 cm^{-1} to the blue when coordinated to Au(I), whereas no changes are expected when the N atom of the pyridine is coordinated to the metal.[43] Adsorption of the dye onto the electrode is further proved by the surface characterization made by photoluminescence measurements. Figure S7 (Supporting Information) shows the photoluminescence spectra recorded for the ZnO nanostructured sample soaked with the Ru complex. When the excitation is performed with the 325 nm line (3.81 eV) of the HeCd source, the typical green luminescence band corresponding to ZnO deep gap state transitions is observed.[44] When the blue line (442 nm) is used to excite the same sample, ZnO cannot be excited because the excitation photon energy (2.81 eV) is significantly lower than the ZnO band gap (3.37 eV) in this case. Hence, the typical ZnO green band is no longer present in the spectrum. In contrast, a new peak at 625 nm, with a shoulder at about 675 nm, is observed, which corresponds to electronic transitions within the Ru complex molecules distributed in the nanostructured ZnO matrix, since complex **1** emits at 623 nm in CH_3CN solution at room temperature (Table 4). The shoulder near 680 nm, which is barely detected at room temperature (Figure S3, Supporting Information), is due to vibronic structure and its intensity is expected to increase when lowering the temperature.[31] Selective excitation of the complex is reasonable, considering that the 442 nm excitation line is very close to the maximum absorption wavelength of complex **1** (454 nm).

Intramolecular Electron Transfer. Although we could not obtain crystals of complex **4**, coordination of pentaammineruthenium(II) to the free N of the nitrile group of Mebpy-CN bonded to $Ru(bpy)_2^{2+}$ moiety is clearly evidenced by IR, CV, NMR, and UV−vis data. A scheme of the structure of the cation is shown in Scheme 2.

As shown in Figure 9, selective oxidation of the pentaammine ruthenium (Ru_a) in **4** either by an electrochemical or a chemical way produces the mixed-valent complex **5**. The band at 518 nm, corresponding to a MLCT ($Ru_a \rightarrow$ Mebpy-CN), disappears and a weak band appears at λ_{max} = 801 nm (ε = 510 $M^{-1}cm^{-1}$), corresponding to a MMCT from Ru_b to Ru_a.

Scheme 2. Structure of the Cation of Complex 4

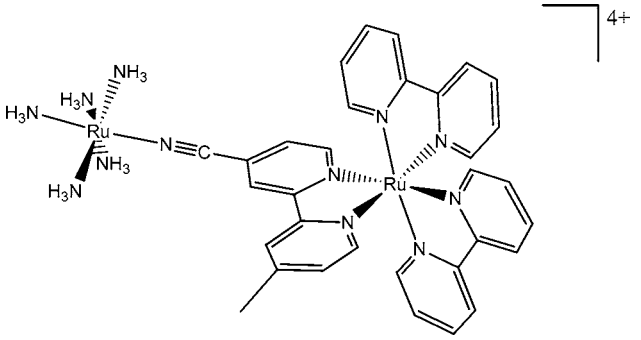

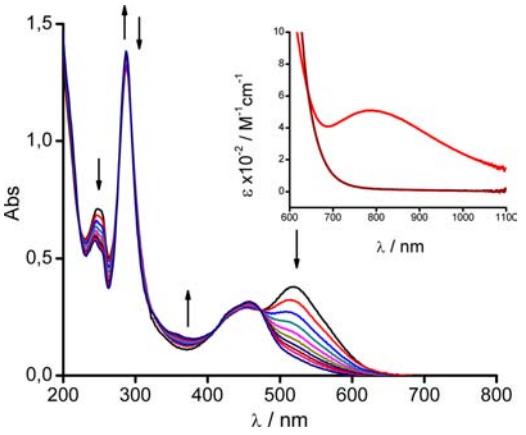

Figure 9. Controlled potential electrolysis of **4** at 1 V vs Ag/AgCl in CH_3CN, the final species being **5**. (Inset) Solution 1.36×10^{-3} M of **4** in CH_3CN (wine-red line) and the same solution after addition of excess Br_2(g) to obtain **5** (red line).

The experimental values of $\tilde{\nu}_{max}$, ε_{max}, and E_{op}, obtained by deconvolution of the Gaussian-shaped MMCT band (Figure 9), were used for calculating the values of H_{AB}, α^2, and λ (electronic coupling, electron delocalization parameter, and reorganization energy for the intramolecular electron transfer, respectively) through eqs 10−12[45]

$$H_{AB}(cm^{-1}) = 2.06 \times 10^{-2}[(\varepsilon_{max})(\tilde{\nu}_{max})(\Delta\tilde{\nu}_{1/2})]^{1/2}(1/r) \quad (10)$$

$$\alpha^2 = (H_{AB}/\tilde{\nu}_{max})^2 \quad (11)$$

$$\lambda = E_{op} - \Delta G^{\circ} - \Delta E_{exc} \quad (12)$$

where ε_{max} is the molar absorptivity at the absorption maximum, $\tilde{\nu}_{max}$ is the energy of the intervalence absorption maximum, $\Delta\tilde{\nu}_{1/2}$ is the bandwidth at half-height of the intervalence transition, r is the metal−metal distance, E_{op} is the energy of the intervalence absorption maximum in eV, ΔG° is the free energy between both redox centers (assumed as approximately $\Delta E_{1/2} = E_{1/2}(Ru_b^{III}/Ru_b^{II}) - E_{1/2}(Ru_a^{III}/Ru_a^{II})$), and ΔE_{exc} is the energy difference between the excited and ground states, estimated as 0.25 eV for several ruthenium complexes in the event that MMCT results in the population of an excited state.[46] The distance r (9.2 Å) was estimated based on the crystal structure of **1** and the typical distance Ar−CN−Ru_a.[9]

The value of the estimated electronic coupling element between both metallic centers, H_{AB} = 390 cm^{-1}, is 2 times higher than that found in a mixed-valent complex with a similar

dx.doi.org/10.1021/ic302594b | Inorg. Chem. 2013, 52, 4950−4962

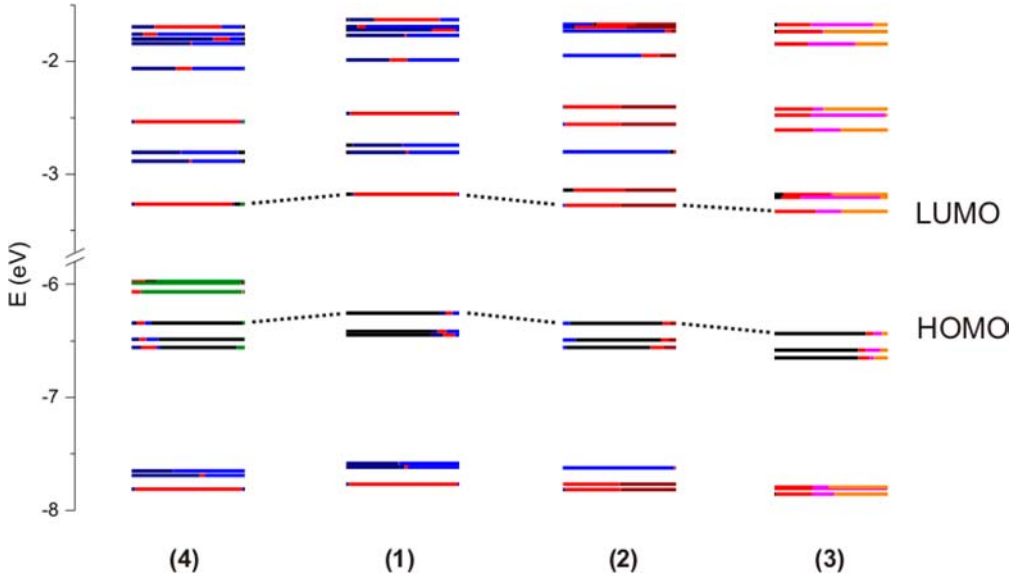

Figure 10. Orbital diagrams calculated by DFT for complexes **1**−**4**. Different contributions of the groups are marked by different colors: bipyridyl ruthenium center in black, pentaammine ruthenium center in green, bpys in blue, and Mebpy-CNs in red. For the values of each contribution, see Table S1 (Supporting Information).

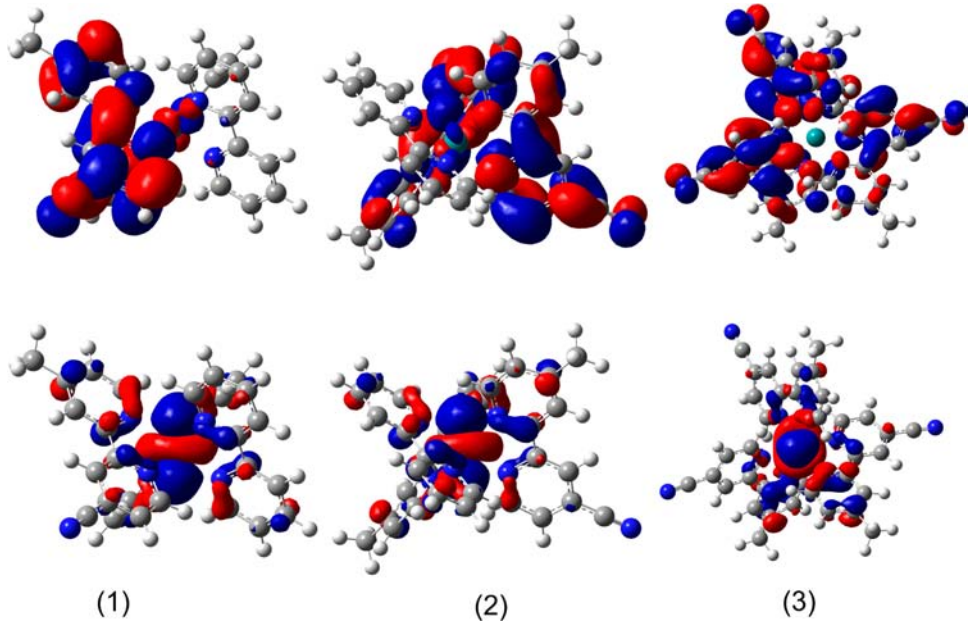

Figure 11. Orbital pictures of LUMOs (top) and HOMOs (bottom) of complexes **1**−**3**.

metal−metal distance of formula $[(bpy)_2Ru(5\text{-}CNphen)Ru(NH_3)_5]^{5+}$ (5-CNphen =5-cyano-1,10-phenanthroline),[9] which can be due to increased conjugation of the Mebpy-CN ring as compared to that of the 5-CNphen ring. The value of α^2 (1.0×10^{-3}) indicates a higher delocalization by almost 1 order of magnitude. The value of the reorganization energy λ (0.60 eV) is less than that of $-\Delta G^\circ$ (0.70 eV), so that the rate constant for the charge recombination step (k_b in Scheme 1) following light excitation ($Ru_a^{II} \rightarrow Ru_b^{III}$) is predicted to fall in the Marcus inverted region.[47] This fact opens up the possibility of having long-lived charge-separated states in mixed-valent species with lower values of λ and higher values of $-\Delta G^\circ$ than those found in this study (using a $Mo(CO)_5$ moiety, for instance, instead of a $Ru(NH_3)_5$ group) and thus shifting closer to the primary steps of photosynthesis.

Calculations. DFT and TD-DFT theories have already been applied successfully in the evaluation of ground and excited state properties of ruthenium(II) polypyridyl complexes.[48] The orbital energy levels of complexes **1**−**4**, calculated by DFT, are shown in Figure 10 and indicate that the LUMOs of all complexes are delocalized over the Mebpy-CN ligands. Calculated orbital energies are consistent with the redox potentials measured by CV and DPV (Table 3) and put into evidence the stabilization of the bipyridyl ligands on going from **1** to **3**. The increasing delocalization on increasing the number of Mebpy-CN ligands explains the stabilization of the LUMO levels. The HOMOs are centered on one of the d orbitals of the Ru_b. Orbital pictures of HOMOs and LUMOs for complexes **1**−**3** are depicted in Figure 11. In complex **4**, the HOMO is centered on Ru_a, as expected. As already reported in the series

dx.doi.org/10.1021/ic302594b | Inorg. Chem. 2013, 52, 4950−4962

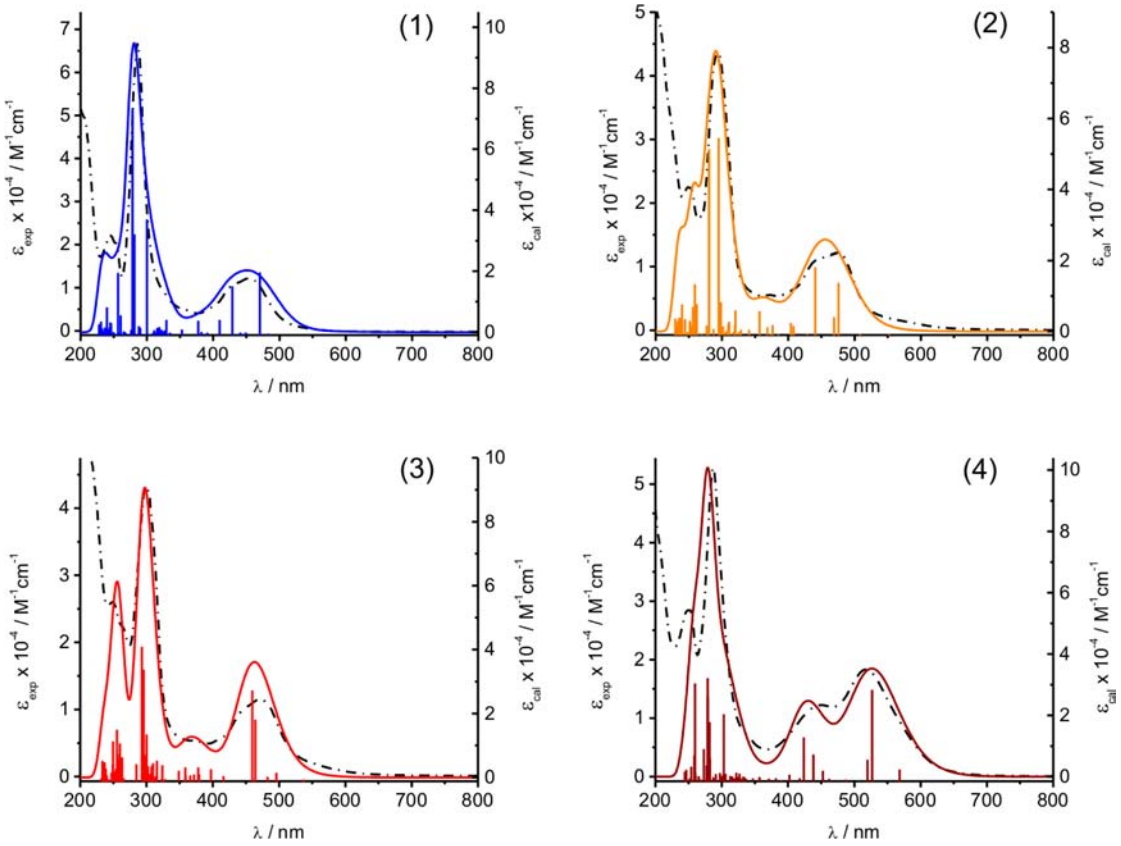

Figure 12. Calculated UV−vis spectra of **1**−**4** (from left to right) in straight lines; experimental spectra in dashed lines.

$[Ru(bpy)_{3-x}(dab)_x]^{2+}$ (x = 0−3), with dab =1,4-diazo-1,3-butadiene,[48] there is a linear relationship between the LUMO and the HOMO energies (Table S1 in Supporting Information) with the number of substituted ligands. This finding is consistent with the correlation of the first oxidation and reduction potentials with HOMO and LUMO energies.

The UV−vis spectra calculated by TD-DFT (Figure 12) are in excellent agreement with the experimental data concerning the maxima of the MLCT and IL bands and relative intensities between the bands. The calculated extinction molar coefficients are overestimated by a factor of around 2. The nature of the transitions obtained by TD-DFT calculations confirms the assignments of the UV−vis bands of these complexes (see Table S2 of Supporting Information).

There is an increase in intensity of the band around 250 nm when going from **1** to **3**. The results of calculated UV−vis spectra indicate that this effect could be due to a second IL transition associated to Mebpy-CN (Figure 12). This band is displaced to lower energies when the ligand is reduced, and thus, we can explain the intensity increment of the band at λ_{max} = 330 nm on the time-resolved differential absorption spectra when going from **1** to **3** (Figure 6).

CONCLUSIONS

Substitution of bpy by Mebpy-CN improves the photosensitizing properties of ruthenium polypyridyl complexes. This effect can be amplified by increasing the number of Mebpy-CN ligands coordinated to the metallic center. In the new series $[Ru(bpy)_{3-x}(Mebpy\text{-}CN)_x]^{2+}$ (x = 1−3), the lifetime and quantum yield of emission of the lowest ^{3}MLCT excited state increase steadily when going from x = 0 to x = 3. Quenching by molecular oxygen of ^{3}MLCT excited states of the three complexes produced singlet molecular oxygen $^1O_2$ with quantum yield values higher than that of $[Ru(bpy)_3]^{2+}$. Moreover, the photoconductivity of ZnO nanowires covered with complex $[Ru(bpy)_2(Mebpy\text{-}CN)](PF_6)_2$ is increased by an order of magnitude, pointing to the feasibility of this species as a component of novel DSSCs based on ZnO nanowires. The carbonitrile group of Mebpy-CN can be also covalently bonded to another metallic center to obtain new dinuclear complexes relevant to intramolecular electron transfer processes. The metal−metal electronic coupling of the novel mixed-valent species $[(bpy)_2Ru^{II}(Mebpy\text{-}CN)Ru^{III}(NH_3)_5]^{5+}$ is significantly higher than that of a related complex with a similar metal−metal distance, while the charge recombination step that follows light excitation is predicted to lie in the Marcus inverted region.

ASSOCIATED CONTENT

Supporting Information

Crystallographic data in cif format, SEM image of ZnO nanowires, NMR data of complex **1**, emission spectra, luminescence decays at 660 nm of complex **2** under argon-, air- and oxygen-saturated CH_3CN solutions, photoconductivity vs wavelength of Ru-soaked ZnO NWs and bare ZnO NWs, Raman spectra and photoluminescence spectra of Ru-soaked ZnO nanowires at 4 K, group contributions to MOs, and nature of UV−visible transitions. This material is available free of charge via the Internet at http://pubs.acs.org.

dx.doi.org/10.1021/ic302594b | Inorg. Chem. 2013, 52, 4950−4962

AUTHOR INFORMATION

Corresponding Author

*Phone:(+54)(381)(4200960). Fax: (+54)(381)(4248169). E-mail: nkatz@fbqf.unt.edu.ar.

Notes

The authors declare no competing financial interest.

ACKNOWLEDGMENTS

We thank CONICET, ANPCyT, and UNT for financial support. J.H.M.O. thanks CONICET for a graduate fellowship. D.C., F.E.M.V., C.D.B., and N.E.K. are Members of the Research Career (CONICET). We thank Dr. Miriam Pérez (UAB) for MS measurements and Dr. L. J. Borrero-González and Prof. F. E. G. Guimarães (IFSC, São Paulo University, Brazil) for valuable help with the PL measurements.

REFERENCES

(1) Grätzel, M. *J. Photochem. Photobiol., C: Photochem. Rev.* **2003**, *4*, 145.
(2) Grätzel, M. *Acc. Chem. Res.* **2009**, *42*, 1788.
(3) Hagfeldt, A.; Boschloo, G.; Sun, L.; Kloo, L.; Petterson, H. *Chem. Rev.* **2010**, *110*, 6595.
(4) Chen, X.; Li, C.; Grätzel, M.; Kostecki, R.; Mao, S. S. *Chem. Soc. Rev.* **2012**, *41*, 7909.
(5) Keis, K.; Bauer, C.; Boschloo, G.; Hagfeldt, A.; Westermark, K.; Resnmo, H.; Siegbahn, H. *J. Photochem. Photobiol., A: Chem.* **2002**, *148*, 57.
(6) Harris, J.; Trotter, K.; Brunschwig, B. S. *J. Phys. Chem. B* **2007**, *111*, 6695.
(7) Sakuragi, Y.; Wang, X.-F.; Miura, H.; Matsui, M.; Yoshida, I. J. *J. Photochem. Photobiol., A: Chem.* **2010**, *216*, 1.
(8) McCusker, C. E.; McCusker, J. K. *Inorg. Chem.* **2011**, *50*, 1656.
(9) Mellace, M. G.; Fagalde, F.; Katz, N. E.; Crivelli, I. G.; Delgadillo, A.; Leiva, A. M.; Loeb, B.; Garland, M. T.; Baggio, R. *Inorg. Chem.* **2004**, *43*, 1100.
(10) Cattaneo, M.; Fagalde, F.; Katz, N. E.; Borsarelli, C. D.; Parella, T. *Eur. J. Inorg. Chem.* **2007**, 5323.
(11) Cattaneo, M.; Fagalde, F.; Borsarelli, C. D.; Katz, N. E. *Inorg. Chem.* **2009**, *48*, 3012.
(12) Martí, C.; Jürgens, O.; Cuenca, O.; Casals, M.; Nonell, S. *J. Photochem. Photobiol., A: Chem.* **1996**, *97*, 11.
(13) Frisch, M. J.; Trucks, G. W.; Schlegel, H. B.; Scuseria, G. E.; Robb, M. A.; Cheeseman, J. R.; Zakrzewski, V. G.; Montgomery, J. A.; Stratman, R. E.; Burant, J. C.; Dapprich, S.; Millam, J. M.; Daniels, A. D.; Kudin, K. N.; Strain, M. C.; Farkas, O.; Tomasi, J.; Barone, V.; Cossi, M.; Cammi, R.; Menucci, B.; Pomelli, C.; Adamo,C.; Clifford, S.;. Ochterski, J.;Petersson, G. A.; Ayala, P. Y.; Cui, Q.; Morokuma, K.; Malick, D. K.; Rabuck, A. D.;. Raghavachari, K.; Foresman, J. B.; Cioslovski, J.; Ortiz, J. V.; Stefanov, B. B.; Liu, G.; Liashenko, A.; Piskorz, P.; Komaromi, I.;Gomperts, R.; Martin, R. L.; Fox, D. J.; Keith, T.; Al-Laham, M. A.; Peng, C. Y.; Nanayakkara, A.; Gonzales, C.; Challacombe, M.; Gill, P. M. W.; Johnson, B.; Chen, W.; Wong, M. W.; Andres, J. L.; Gonzales, C.;Head-Gordon, M.; Replogle,E. S.; Pople, J. A. *Gaussian 98*, Revision A.6; Gaussian, Inc.: Pittsburgh, PA, 1998.
(14) Becke, A. D. *J. Chem. Phys.* **1993**, *98*, 5648.
(15) Lee, C.; Yang, W.; Parr, R. G. *Phys. Rev. B* **1988**, *37*, 785.
(16) O'Boyle, N. M.; Tenderholt, A. L.; Langner, K. M. *J. Comput. Chem.* **2008**, *29*, 839.
(17) Gorelsky, S. I.; Lever, A. B. P. *J. Organomet. Chem.* **2001**, *635*, 187.
(18) Monat, J. E.; Rodriguez, J. H.; McCusker, J. K. *J. Phys. Chem. A.* **2002**, *106*, 7399.
(19) *SMART*, Version 5.631; Bruker AXS Inc.: Madison, WI, 1997−2002.
(20) *SAINT+*, Version 6.36A; Bruker AXS Inc.: Madison, WI, 2001.
(21) *SADABS*, Version 2.10; Bruker Advanced X-ray Solutions, 2001. Sheldrick, G. M. *Empirical Absorption Correction Program*; Universität Göttingen: Göttingen: Germany, 1996.
(22) *SHELXTL*, Version 6.14; Bruker Advanced X-ray Solutions, 2000−2003. Sheldrick, G. M. *Program for Crystal Structure Refinement*; Universität Göttingen: Göttingen: Germany, 1997.
(23) (a) Vériot, G.; Dutasta, J.-P.; Matouzenko, G.; Collet, A. *Tetrahedron* **1995**, *51*, 389. (b) Kirby, J. P.; Roberts, J. A; Nocera, D. G. *J. Am. Chem. Soc.* **1997**, *119*, 9230.
(24) Sullivan, B. P.; Salmon, D. J.; Meyer, T. *J. Inorg. Chem.* **1978**, *17*, 3334.
(25) Sutton, J. E.; Taube, H. *Inorg. Chem.* **1981**, *20*, 3125.
(26) Comedi, D.; Tirado, M.; Zapata, C.; Heluani, S. P.; Villafuerte, M.; Mohseni, P. K.; LaPierre, R. R. *J. Alloys Compd.* **2010**, *495*, 439.
(27) Keene, F. R. *Coord. Chem. Rev.* **1997**, *166*, 121.
(28) Shin, Y-g. K.; Szalda, D. J.; Brunschwig, B. S.; Creutz, C.; Sutin, N. *Inorg. Chem.* **1997**, *36*, 3190.
(29) Allen, F. H.; Kennard, O.; Watson, D. G.; Brammer, L.; Orpen, A. G.; Taylor, R. *J. Chem. Soc., Perkin Trans. II* **1987**, S1−S19.
(30) Farrugia, L. J. *ORTEP-3 for windows*, version 1.08; University of Glasgow: Glasgow, 2005.
(31) Juris, A.; Balzani, V.; Barigelletti, F.; Campagna, S.; Belser, P.; Zelewsky, A. V. *Coord. Chem. Rev.* **1988**, *84*, 85.
(32) Dodsworth, E. S.; Lever, A. B. P. *Chem. Phys. Lett.* **1984**, *112*, 567.
(33) Ishida, H.; Tobita, S.; Hasegawa, Y.; Katoh, R.; Nozaki, K. *Coord. Chem. Rev.* **2010**, *254*, 2449.
(34) O'Neill, L.; Perdisatt, L.; O'Connor, C. *J. Phys. Chem. A* **2012**, *116*, 10718.
(35) Abdel-Shafi, A. A.; Beer, P. D.; Mortimer, R. J.; Wilkinson, F. *Helv. Chim. Acta* **2001**, *84*, 2784.
(36) Borsarelli, C. D.; Braslavsky, S. E. *J. Photochem. Photobiol., B: Biol.* **1998**, *43*, 222.
(37) Wilkinson, F. *Pure Appl. Chem.* **1997**, *69*, 851.
(38) Gijzeman, O. L. J.; Koufman, F.; Porter, G. *J. Chem. Soc., Faraday Trans. 2* **1973**, *69*, 708.
(39) Abdel-Shafi, A. A.; Ward, M. D.; Schmidt, R. *Dalton Trans.* **2007**, 2517.
(40) Studenikin, S. A; Golego, N.; Cocivera, M. *J. Appl. Phys.* **1998**, *84*, 5001.
(41) Hau, J.; Fan, F.; Xu, C.; Lin, S.; Wei, M.; Duan, X.; Wang, Z. L. *Nanotechnology* **2010**, *21*, 405203.
(42) Nguyen, H.-M.; Mane, R. S.; Ganesh, T.; Han, S.-H.; Kim, N. *J. Phys. Chem. C* **2009**, *113*, 9206.
(43) Farha, F., Jr.; Iwamoto, R. T. *Inorg. Chem.* **1965**, *4*, 844.
(44) (a) Grinblat, G.; Capeluto, M. G.; Tirado, M.; Bragas, A. V.; Comedi, D. *Appl. Phys. Lett.* **2012**, 233116. (b) Vega, N. C.; Wallar, R.; Caram, J.; Grinblat, G.; Tirado, M.; LaPierre, R. R.; Comedi, D. *Nanotechnology* **2012**, *23*, 275602.
(45) Creutz, C. *Prog. Inorg. Chem.* **1983**, *30*, 1.
(46) Katz, N. E.; Creutz, C.; Sutin, N. *Inorg. Chem.* **1988**, *27*, 1687.
(47) Marcus, R. A.; Sutin, N. *Biochim. Biophys. Acta* **1985**, *811*, 265.
(48) Guillon, T.; Boggio-Pasqua, M.; Alary, F.; Heully, J.-L; Lebon, E.; Sutra, P.; Igau, A. *Inorg. Chem.* **2010**, *49*, 8862.